

## Article

# Work Function, Sputtering Yield and Microhardness of an Al-Mg Metal-Matrix Nanostructured Composite Obtained with High-Pressure Torsion

Rinat Kh. Khisamov<sup>1</sup>, Ruslan U. Shayakhmetov<sup>1</sup>, Yulay M. Yumaguzin<sup>1,2</sup>, Andrey A. Kistanov<sup>1,3,\*</sup>, Galiia F. Korznikova<sup>1,\*</sup>, Elena A. Korznikova<sup>1,3</sup>, Konstantin S. Nazarov<sup>1</sup>, Gulnara R. Khalikova<sup>1,4</sup>, Rasim R. Timiryayev<sup>1</sup> and Radik R. Mulyukov<sup>1,2</sup>

<sup>1</sup> Institute for Metals Superplasticity Problems, Russian Academy of Sciences, Ufa 450001, Russia

<sup>2</sup> Institute of Physics and Technology, Ufa University of Science and Technology, Ufa 450076, Russia

<sup>3</sup> The Laboratory of Metals and Alloys Under Extreme Impacts, Ufa University of Science and Technology, Ufa 450076, Russia

<sup>4</sup> Ufa State Petroleum Technological University, Ufa 450062, Russia

\* Correspondence: andrei.kistanov.ufa@gmail.com (A.A.K.); gfkornikova@gmail.com (G.F.K.)

**Abstract:** Severe plastic deformation has proven to be a promising method for the in situ manufacturing of metal-matrix composites with improved properties. Recent investigations have revealed a severe mixing of elements, as well as the formation of non-equilibrium intermetallic phases, which are known to affect physical and mechanical properties. In this work, a multilayered aluminum-magnesium (Al-Mg) nanostructured composite was fabricated using constrained high-pressure torsion (HPT) in a Bridgeman-anvil-type unit. A microstructure investigation and X-ray diffraction analysis allowed us to identify the presence of intermetallic Al<sub>3</sub>Mg<sub>2</sub> and Al<sub>12</sub>Mg<sub>17</sub> phases in the deformed nanostructured composite. The sputtering yield of the Al<sub>3</sub>Mg<sub>2</sub> and Al<sub>12</sub>Mg<sub>17</sub> phases was found to be 2.2 atom/ion and 1.9 at/ion, respectively, which is lower than that of Mg (2.6 at/ion). According to density functional theory (DFT)-based calculations, this is due to the higher surface-binding energy of the intermetallic phases (3.90–4.02 eV with the Al atom removed and 1.53–1.71 eV with the Mg atom removed) compared with pure Al (3.40–3.84 eV) and Mg (1.56–1.57 eV). In addition, DFT calculations were utilized to calculate the work functions (WFs) of pure Al and Mg and the intermetallic Al<sub>3</sub>Mg<sub>2</sub> and Al<sub>12</sub>Mg<sub>17</sub> phases. The WF of the obtained Al-Mg nanostructured composite was found to be 4 eV, which is between the WF value of Al (4.3 eV) and Mg (3.6 eV). The WF of the Al<sub>12</sub>Mg<sub>17</sub> phase was found to be in a range of 3.63–3.75 eV. These results are in close agreement with the experimentally measured WF of the metal matrix composite (MMC). Therefore, an intermetallic alloy based on Al<sub>12</sub>Mg<sub>17</sub> is proposed as a promising cathode material for various gas-discharge devices, while an intermetallic alloy based on Al<sub>3</sub>Mg<sub>2</sub> is suggested as a promising optical- and acoustic-absorbing material.

**Keywords:** Al-Mg composite; high-pressure torsion; microstructure; microhardness; work function; sputtering yield; ion irradiation



**Citation:** Khisamov, R.K.; Shayakhmetov, R.U.; Yumaguzin, Y.M.; Kistanov, A.A.; Korznikova, G.F.; Korznikova, E.A.; Nazarov, K.S.; Khalikova, G.R.; Timiryayev, R.R.; Mulyukov, R.R. Work Function, Sputtering Yield and Microhardness of an Al-Mg Metal-Matrix Nanostructured Composite Obtained with High-Pressure Torsion. *Appl. Sci.* **2023**, *13*, 5007. <https://doi.org/10.3390/app13085007>

Academic Editor: Theodore E. Matikas

Received: 25 March 2023

Revised: 12 April 2023

Accepted: 14 April 2023

Published: 16 April 2023



**Copyright:** © 2023 by the authors. Licensee MDPI, Basel, Switzerland. This article is an open access article distributed under the terms and conditions of the Creative Commons Attribution (CC BY) license (<https://creativecommons.org/licenses/by/4.0/>).

## 1. Introduction

Al-Mg-based alloys are widely used in industry. However, modern technologies require the use of new / modified materials with improved physical and mechanical properties. For example, such materials with enhanced properties are metal-matrix composites [1–5]. Among those, the application area of composites based on Al-Mg can be found in the automotive, marine, aerospace and electronics industries. The use of such composites in electrovacuum devices—in particular, as cathode (electron emitter) materials in gas-discharge devices, plasma installations, ion sources, sputtering systems, etc.—can also be considered. Since the cathodes in such devices operate under gas discharge conditions, the

cathode's material should have a low-value electron WF and a low sputtering rate. In this regard, studies of the WF and sputtering rate of Al-Mg composites are of practical interest.

The production of MMCs typically involves a combination of two or more materials with different properties, which are then mixed and processed to create a uniform distribution of the dispersed phase in the metallic matrix. One of the most common methods for producing MMCs is through powder metallurgy, which involves mixing the powders of the matrix and dispersed materials, followed by compaction and sintering. Another method is liquid-metal infiltration, in which a porous preform made of the dispersed phase is infiltrated with molten metal to create the composite. One may also recall such methods as spray forming, squeeze or stir casting [6], accumulative roll bonding [7], explosive bonding [8], friction stir welding, powder technologies, etc.

However, severe plastic deformation (SPD) has emerged as a promising method for the in situ manufacturing of MMCs with improved properties. SPD processes, such as high-pressure torsion (HPT), impose large strains on the material, leading to severe deformation and the mixing of the materials at the atomic level. HPT is a popular SPD process that involves subjecting a sample to a torsional shear under high pressure in a confined space, which leads to the plastic deformation and homogenization of the material. MMCs obtained via SPD processes have improved mechanical and physical properties compared with conventionally produced MMCs, making them a promising area of research and development [9–11]. HPT is characterized by the highest shear strains in a material without fractures [12]. This method has been used for the manufacturing of homogeneous composite structures in Al-Cu [9,13,14], Al-Ti [15,16], Al-Mg [17,18] and various other systems, even including as dissimilar a combination as Al-Nb [19]. The main advantage of the HPT process is the possibility of manufacturing composites without contamination and residual porosity in one step at room temperature.

Several studies have investigated the fabrication and properties of Al-based MMCs produced with HPT. For instance, one study reports the creation of an aluminum-based composite material reinforced with SiC particles through HPT [20]. The material exhibited enhanced wear resistance and mechanical properties compared with the base alloy. Another study describes the fabrication of an MMC using HPT on Al and aluminum oxide powders [21]. The resulting material showed improved hardness and compressive strength compared with pure Al. The addition of nanoparticles to the matrix has also been investigated to improve the properties of MMCs produced with HPT. In one study, an Al-Mg alloy reinforced with TiB<sub>2</sub> nanoparticles was fabricated using HPT, and the results showed improved mechanical properties and wear resistance [22]. Similarly, Al-graphene oxide composites were fabricated with HPT, and the material exhibited enhanced strength and ductility compared with the base aluminum [23]. The use of different reinforcing particles, such as nano-SiC particles [24], carbon nanotubes [25], alumina particles [26] and TiC particles [27], has also been investigated to improve the properties of Al-based MMCs produced with HPT. In each case, the resulting material showed improved mechanical properties compared with the base Al. Furthermore, the microstructure and mechanical properties of Al-based composites reinforced with ceramic particles, such as SiC [28], Si<sub>3</sub>N<sub>4</sub> [29] and TiN [30], were investigated by using HPT. In each case, HPT improved the mechanical properties of the composite.

Overall, these studies demonstrate the potential of HPT as an effective method for producing MMCs with enhanced mechanical properties. The use of different reinforcing particles and processing parameters in HPT can lead to further improvements in the properties of MMCs. Further research is needed to investigate the behavior of these MMCs under different loading conditions and optimize their processing parameters for various applications.

The aim of the work is to investigate the effect of severe plastic deformation on the properties of a multilayered Al-Mg nanostructured composite. The motivation for the study is to explore new manufacturing methods for MMCs that can result in improved properties. The study focuses on the analysis of the microstructure of the composite, particularly the

presence of the intermetallic phases  $\text{Al}_3\text{Mg}_2$  and  $\text{Al}_{12}\text{Mg}_{17}$ , which are known to affect a composite's physical and mechanical properties. The novelty of the study is in the use of constrained HPT to fabricate the nanostructured composite and the application of DFT modeling to calculate the work functions of pure metals and intermetallic phases.

## 2. Materials and Methods

Al (1050) and Mg (AZ31) billets with a grain size of about 10  $\mu\text{m}$  were utilized as the workpiece material in this work. Samples of Al and Mg of 12 mm in diameter and with a thickness of 1 mm and 0.3 mm, respectively, were placed in an Al-Mg-Al sequence on Bridgman anvils with grooves in their centers of 12 mm in diameter and a depth of 0.25 mm. The specimens were subjected to high-pressure torsion under 5 GPa of pressure for 10 revolutions at room temperature, as described in [18]. As a result, a disk-shaped Al-Mg sample was obtained with a diameter of 12 mm and a thickness of 0.6 mm. To increase the fraction of intermetallic phases in the nanostructured composite, the HPT sample was annealed in a vacuum at 275  $^\circ\text{C}$  for 30 min. Further analysis of the microstructure and properties was carried out on the surface of the Al-Mg disk. For this purpose, the outer Al layer of the sample was removed by grinding and polishing it until Mg inclusions were revealed on the flat surface. The surface roughness,  $R_a$ , was evaluated using an LSM-5 Exciter laser scanning microscope (Carl Zeiss) and found to be lower than 0.3  $\mu\text{m}$ . The phase composition of the surface was analyzed using a Rigaku Ultima IV X-ray diffractometer using Cu-K $\alpha$  radiation. The phase content was quantified via Rietveld analysis with an accuracy of 0.1%. The microstructure was examined using a Mira 3LHM scanning electron microscope (SEM) (Tescan) combined with an energy-dispersive X-ray spectroscopy (EDX) analyzer (Oxford Instruments, Oxford, Great Britain).  $\text{Al}_3\text{Mg}_2$  and  $\text{Al}_{12}\text{Mg}_{17}$  are the main intermetallic compounds formed at the Al-Mg interface in various joining and bonding processes of these light metals [31–33]. These intermetallic compounds and their structures determine the efficiency of the joint since the precipitation of the  $\text{Al}_{12}\text{Mg}_{17}$  and the  $\text{Al}_3\text{Mg}_2$  phases has a strengthening effect.

The WF of the Al-Mg sample was measured as the contact potential difference, obtained via the Kelvin–Zisman method (vibrating electrode technique) [34–36]. Samples of the initial billets of Al and Mg were utilized for comparison. A platinum plate with an area of 3  $\times$  3  $\text{mm}^2$  was used as a vibrating electrode. A low-frequency generator was used to set the resonant oscillation frequency to  $\approx$ 200 Hz. An alternating electrical signal was observed between the vibrating electrode and the studied sample when close in distance. The signal was amplified and analyzed using an amplitude–frequency spectrometer. By applying a negative bias voltage to the sample under study relative to the Pt electrode, the signal amplitude in the spectrum decreased from its maximum value to zero. The value of the bias voltage corresponded to the value of the contact potential difference between the Pt electrode and the sample under study.

The WF of the studied Al-Mg nanostructured composite was also calculated from the first principles in the framework of the DFT using the plane-wave Vienna Ab initio Simulation Package (VASP) [37]. The first Brillouin zone was sampled with a 20  $\times$  20  $\times$  10 k-mesh grid, and a vacuum space of 15  $\text{Å}$  was set in the direction perpendicular to the surface plane. The kinetic energy cutoff for the plane wave expansion was set to 520 eV. All the considered structures were fully optimized until the atomic forces and total energy values were smaller than 10<sup>−4</sup> eV/ $\text{Å}$  and 10<sup>−8</sup> eV, respectively.

To determine the sputter rates and yields of the  $\text{Al}_3\text{Mg}_2$ ;  $\text{Al}_{12}\text{Mg}_{17}$ ; intermetallic phases; and Al and Mg metals, an Al-Mg sample was subjected to ion irradiation. Irradiation was carried out with argon ions with an energy of 5 keV, normal to the disk surface. The disc was placed in an ion-beam setup with an ion source with a closed electron drift APEL-IS-CELL (Applied Electronics). The ion current density was set as equal to 0.5 mA/ $\text{cm}^2$ , and the exposure time was 3 h. The sample temperature during irradiation was  $\leq$ 100  $^\circ\text{C}$ . The surface of the irradiated sample was examined using a Mira 3LHM and Nanoscan-3D microscope (Tisnum) in the atomic force microscope mode.

The Vickers microhardness of the irradiated sample's surface was measured at a load of 5 g using an MHT-10 microhardness tester (Paar Physica) combined with an Axiovert-100 A (Carl Zeiss) optical microscope.

The microhardness was measured using an optical microscope where a region on the surface of the composite sample containing phases of Al; Mg; and intermetallic  $\text{Al}_3\text{Mg}_2$  and  $\text{Al}_{12}\text{Mg}_{17}$  layers was identified. Impressions were made on the surface of each phase using a four-sided diamond pyramid with a load of 5 g (0.05 Newtons) for 10 s. The surface with the impressions was examined using an optical microscope. The microhardness value of each phase was determined from measurements of the diagonal of at least four imprints, which were processed using the MHT-10 microhardness tester software.

For comparison, the microhardness of the non-irradiated surface on the reverse side of the sample was measured. For that, the reverse side of the sample was ground and polished to remove the Al layer until Mg inclusions were revealed on the surface.

### 3. Results and Discussion

#### 3.1. Microstructure and Phase Characterization of the HPT Processed Composite

##### 3.1.1. XRD

The indexed XRD patterns of the Al, Mg and Al–Mg nanostructured composites after HPT and following annealing at 275 °C are shown in Figure 1. The HPT samples were primarily characterized by the presence of fcc Al (92.4 wt.%) and hcp Mg (7.6%) (see Figure 1).  $\text{Al}_3\text{Mg}_2$  and  $\text{Al}_{12}\text{Mg}_{17}$  intermetallic phases, alongside Al and Mg, were observed in the HPT sample after annealing (see Figure 1). The sample's surface phase composition was found to be as follows (wt.%): 74.3 Al, 3.2 Mg, 19.1  $\text{Al}_3\text{Mg}_2$  and 3.4  $\text{Al}_{12}\text{Mg}_{17}$ . A detailed analysis of the intermetallic growth kinetics during annealing in the Al-based metal-matrix composites fabricated with HPT is provided in the authors' previous works [14].

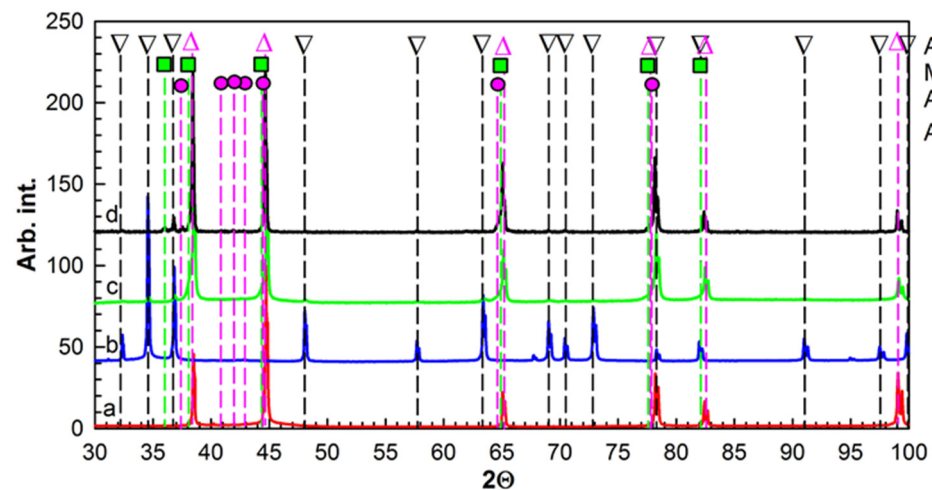


**Figure 1.** XRD patterns of Al (a), Mg (b) and Al-Mg nanostructured composites under HPT conditions (c) and after further annealing at 275 °C (d).

Our observation is consistent with the results of explosion welding Al-Mg claddings, where, in the state immediately after explosion welding, intermetallic phases were not observed, and the use of annealing led to the formation of the intermetallic compounds  $\text{Al}_3\text{Mg}_2$  and  $\text{Al}_{12}\text{Mg}_{17}$  [38].

An analysis of the Al XRD profiles broadening is summarized in Table 1. It can be seen that the lattice parameter in the as-deformed condition is larger than that of undeformed pure Al (i.e.,  $a = 4.0494 \text{ \AA}$ ). Pure Al is widely known to be subject to dynamic recrystallization under severe strains due to its high stacking-fault energy and high deformation-to-melting ratio (homologous) temperature, and one can conclude that the HPT-induced increase in the Al lattice parameter in the composite was caused by the formation of an

Al–Mg solid solution. In general, the value of the coherent scattering domain, as well as the values of the lattice parameters and microstrains, corresponds to the values obtained in the HPT-processed pure Al. Annealing at 150 °C led to some relaxation of the Al matrix structure—the lattice parameter was partially restored, and the level of microstrains was decreased. Annealing at 275 °C resulted in the lattice parameter being almost restored, and the microstress value came to an equilibrium.

**Table 1.** Lattice parameter, coherent scattering domain and lattice microstrains of the Al–Mg composite after HPT and subsequent annealing at 150 and 275 °C.

State	Lattice Parameter, Å	Coherent Scattering Domain, nm	Lattice Microstrains, %
As-deformed HPT Al-Mg	4.05093(2)	55	0.092
HPT Al-Mg + annealing 150 °C	4.050034(4)	400	0.031
HPT Al-Mg + annealing 275 °C	4.049829(2)	550	0.025

### 3.1.2. SEM Analysis

Following SEM analysis, the Al–Mg nanostructured composite was found to consist of an Al matrix with isolated Mg inclusions (Figure 2). Two interlayers were found between Al and Mg arrays with a different color contrast from that of the Al and Mg phases. As an outcome of EDX analysis, the chemical composition of the first layer, co-joined with Al, consisted of Al-60 at. % and Mg-40 at. %. The latter corresponds to the  $\text{Al}_3\text{Mg}_2$  intermetallic phase. The composition of the second layer, co-joined between the first layer on one side and Mg on the other side, consisted of about Al-40 at. % and Mg-60 at. %. This approximately corresponded to the  $\text{Al}_{12}\text{Mg}_{17}$  phase. The detailed element composition of the interlayers at the interphase boundaries between Al and Mg is provided hereafter. A direct correspondence between the stoichiometric phases' compositions and the atomic distribution of the obtained EDX cannot be observed due to the small size of the particles and their localized nature. This prevented the estimation of the components' atomic ratio with high accuracy.

### 3.2. WF Measurements

The value of the potential difference between the Pt (vibrating electrode) and Al was found to be  $1.0 \pm 0.1$  V, and it was  $1.7 \pm 0.2$  V between Pt and Mg. Assuming the value of the WF of Pt to be equal to 5.3 eV [39], the WF of Al was found to be  $4.3 \pm 0.1$  eV, and the WF of Mg was  $3.6 \pm 0.2$  eV (Table 2). The obtained values were in good agreement with the data on the WF of Al and Mg presented in [39–41]. To confirm the obtained results, measurements of the Pt sample were carried out. The potential difference for Pt was found to be 0.1 eV, which supported the reliability of the performed measurements and results.

**Table 2.** Contact potential difference and WF of Al, Mg and Al–Mg composites measured in relation to the WF of Pt, considered to be equal to 5.3 eV [18], using the Kelvin–Zisman method (vibrating electrode method).

Sample	Contact Potential Difference, V	WF, eV (Relative to Pt = 5.3 eV)
Al	1.0	4.3
Al-Mg composite	1.3	4.0
Mg	1.7	3.6
Pt	0.1	-

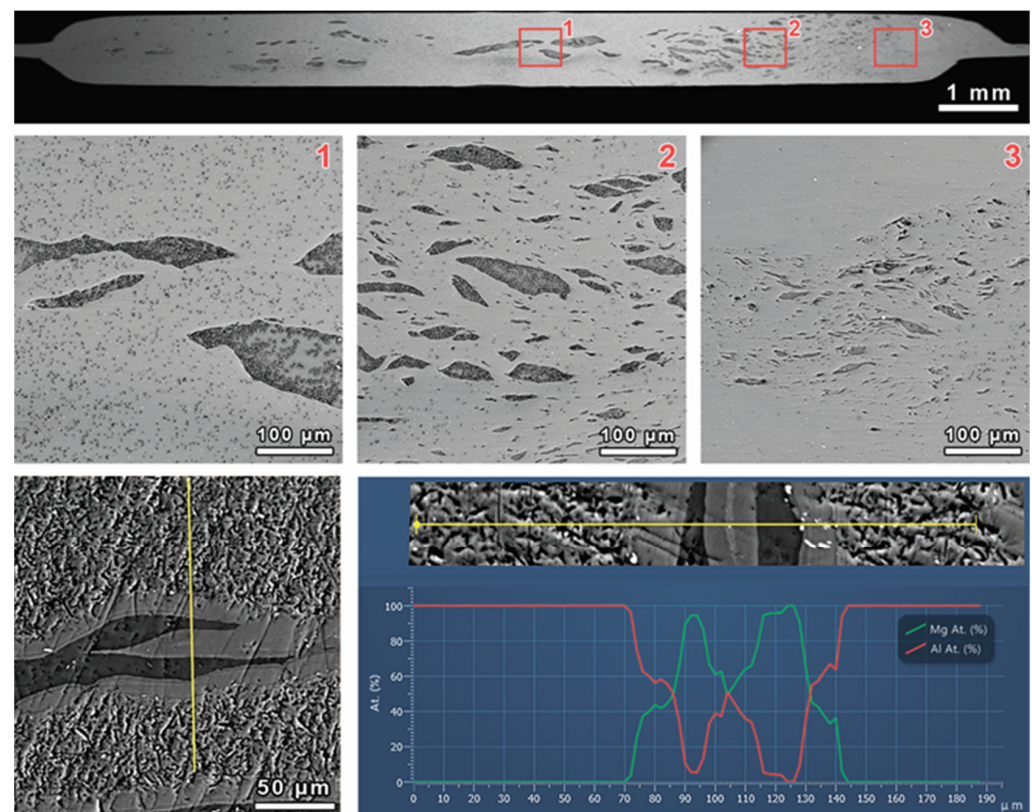


**Figure 2.** SEM images (BSE mode) of the Al-Mg nanostructured composite cross-section at different magnifications and element distribution along the line shown at the top of the panel in the form of a relative intensity plot in relation to the scanning distance of the Mg and Al, marked by green and red, respectively.

As noted above, the surface of the Al-Mg nanostructured composite was characterized by an Al matrix with isolated Mg inclusions, as well as interlayers of intermetallic phases at the interphase boundaries. Since the sample surface was inhomogeneous in its chemical composition, measurements of the contact potential difference were carried out for the entire sample. For that, the surface of different sections, i.e., the center, the middle and the edge of the sample, were substituted under a vibrating electrode with an area of  $3 \times 3 \text{ mm}^2$ . The values of the contact potential differences over the surface of the entire Al-Mg sample ranged from 1.24 to 1.36 V, which, on average, resulted in a value of 1.3 V. Therefore, the value of the WF of the Al-Mg nanostructured composite was  $\approx 4.0 \text{ eV}$ , which was between the WF values of Al and Mg.

### 3.3. WF Calculations

The integral WF of a chemically inhomogeneous surface is known to be equal to the sum of the WFs of chemical elements depending on their areas on the surface; i.e.,  $WF = WF_1S_1 + WF_2S_2 + \dots + WF_nS_n$ , where  $WF_1$ ,  $WF_2$  and  $WF_n$  are the local values of the WFs of chemical elements, and  $S_1$ ,  $S_2$ ,  $\dots$   $S_n$  are the relative areas of the chemical elements on the surface [42]. The WF value of the Al-Mg nanostructured composite, which was mentioned to be between the WF values of Al and Mg, is induced not only by these metals but also by the contribution of the WF of the  $\text{Al}_3\text{Mg}_2$  and  $\text{Al}_{12}\text{Mg}_{17}$  intermetallic phases. The WF values of the  $\text{Al}_{12}\text{Mg}_{17}$  intermetallic phase and Al and Mg metals were determined using DFT calculations.

Due to the complexity of the  $\text{Al}_3\text{Mg}_2$  phase lattice, consisting of a large number of atoms [3], the WF calculation of this phase using the DFT method was difficult. The WF was calculated for the  $\text{Al}_{30}\text{Mg}_{23}$  phase [43] with a composition close to the  $\text{Al}_3\text{Mg}_2$  phase. The atomic structures of these phases were taken from open databases [44]. The WF calculations

of the Al, Mg and intermetallic phases were carried out for low-index planes (001), (101) and (111), corresponding to the *fcc* lattice.

The results of the WF calculations are summarized in Table 3. The lowest WF of Mg and the highest WF of Al were in agreement with the WF values of Al and Mg presented elsewhere [41]. The calculated WF values for the Al<sub>12</sub>Mg<sub>17</sub> and Al<sub>30</sub>Mg<sub>23</sub> phases were found to be in between those of Al and Mg (Table 3). The integral WF of the Al-Mg sample was calculated considering the relative weight concentration and the smallest/largest WF values (see Table 3) of every existing phase on its surface. In the case of the smallest WF values, the integral WF was 4.0 eV, while for the largest WF values, the integral WF was 4.1 eV. This result was found to correlate with the experimentally measured WF of the Al-Mg sample.

**Table 3.** The values of the electron WFs of the Al, Mg and Al<sub>12</sub>Mg<sub>17</sub> and Al<sub>30</sub>Mg<sub>23</sub> intermetallic phases calculated via the DFT method.

Metal		Our Calculated WF, eV	Other Theoretical Results of WF, eV [22]	Experimental Results of WF, eV [22]
Al	(001)	4.20	4.41, 4.38	4.41
	(101)	4.21	4.08, 4.30	4.28
	(111)	4.08	4.36, 4.25	4.24
Al <sub>12</sub> Mg <sub>17</sub>	(001)→(0001)	3.63	-	-
	(111)→(11-21)	3.75	-	-
Al <sub>30</sub> Mg <sub>23</sub>	(001)→(0001)	3.77	-	-
	(111)→(11-21)	3.85	-	-
Mg	(001)→(0001)	3.6	3.79	3.65 ÷ 3.84
	(101)→(10-11)	3.39	3.70 ÷ 3.80	-
	(111)→(11-21)	3.67	3.56 ÷ 3.68	3.66

### 3.4. Surface Structure Modification as a Result of Ion Irradiation

As a result of ion irradiation, the initially smooth surface of the Al-Mg sample was transformed. An etched Al matrix and etched isolated Mg inclusions were observed on the sample surface (Figure 3). Mg inclusions were found to be more susceptible to etching; i.e., more deep etching was observed compared with the Al matrix.

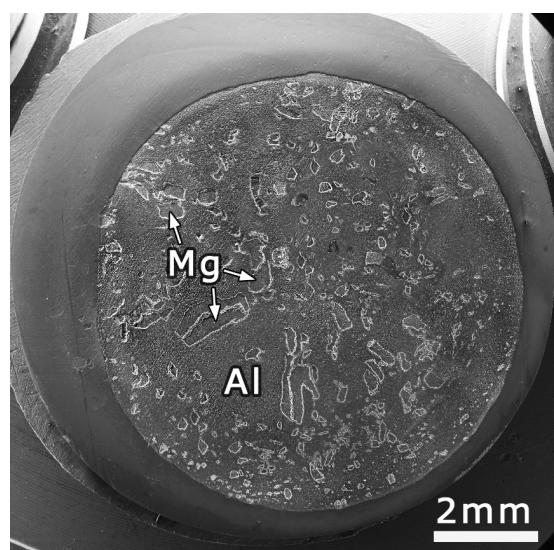


**Figure 3.** SEM image (SE mode) of the surface of the Al-Mg nanostructured composite after HPT and annealing following ion irradiation.

Different morphologies of the Al and Mg areas and interlayers of the  $\text{Al}_3\text{Mg}_2$  and  $\text{Al}_{12}\text{Mg}_{17}$  intermetallic phases were revealed via SEM at higher magnifications (Figure 4). Etching pits with a diameter of up to  $10\ \mu\text{m}$  formed on the Al surface. Cones with a concentration of  $100\text{--}200\ \text{cones}/\mu\text{m}^2$  were formed on the Mg surface. As a result of irradiation, a relief similar to a cellular wall structure was formed on the surface corresponding to the  $\text{Al}_3\text{Mg}_2$  intermetallic phase. Within the cellular wall structure, curved structures similar to fibers were located. The interlayer corresponding to the  $\text{Al}_{12}\text{Mg}_{17}$  phase had a smooth surface after irradiation. On the lateral side of the  $\text{Al}_{12}\text{Mg}_{17}$  phase interlayer, fibers oriented along the plane of the sample were observed.

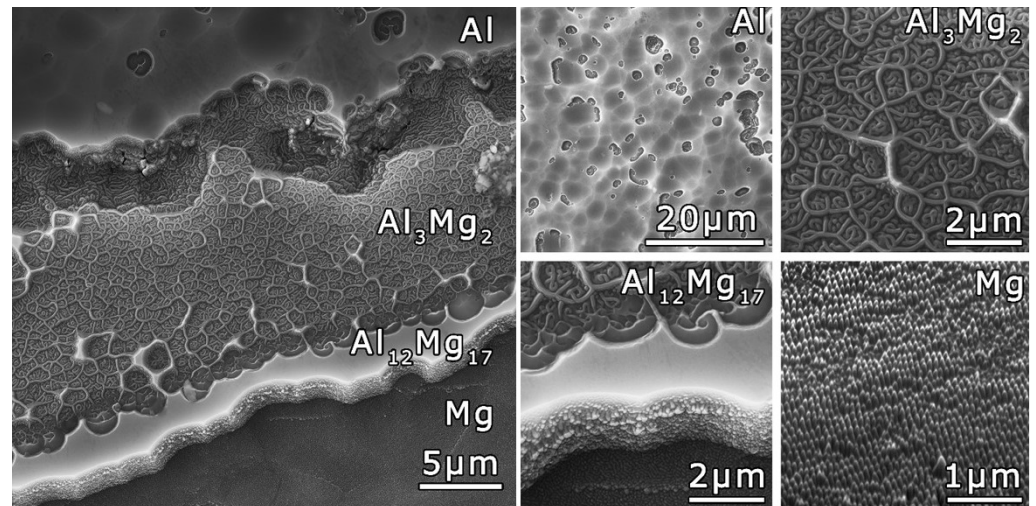


**Figure 4.** SEM images (SE mode) of the Al-Mg nanostructured composite surface after ion irradiation. Tilt angle is  $45^\circ$ .

The formation of various surface morphologies during ion irradiation is known to depend on the irradiation conditions, i.e., dose, fluence and ion energy and the nature of the material and its temperature during irradiation. The simultaneous formation of etch pits on the Al surface and cones on the Mg surface under the same irradiation conditions was the result of the difference in the crystal structure and lattice type of these metals [45]. The difference in the relief formed as a result of ion irradiation on the surface of the interlayers, which corresponded to the  $\text{Al}_3\text{Mg}_2$  and  $\text{Al}_{12}\text{Mg}_{17}$  intermetallic phases, can also be associated with the difference in the crystal structure and lattice type of these phases.

Figure 5 shows the SEM images combined with the EDX map and the element composition profile of the Al-Mg sample surface area after irradiation (Figure 4). Given the measured profiles and the corresponding chemical compositions, it can be seen that the etched areas with different reliefs on the surface of the irradiated composite sample corresponded to Al (line 1), Mg (line 4) and the interlayers of the  $\text{Al}_3\text{Mg}_2$  (line 2) and  $\text{Al}_{12}\text{Mg}_{17}$  (line 3) intermetallic phases. As a result of a detailed analysis of the interlayer corresponding to the  $\text{Al}_3\text{Mg}_2$  intermetallic phase, the wall chemical composition of the cellular wall structure was found to be predominantly Al. On the other hand, the curved fibers inside the honeycomb wall structure were expected to be Mg in the first approximation. Based on the profile of the  $\text{Al}_3\text{Mg}_2$  phase's chemical composition (profile 2 in Figure 5), the protruding walls on the SEM image corresponded to an increase in the Al concentration relative to the general profile of the Mg, whereas fibrous structures corresponded to an increase in the Mg concentration relative to the Al concentration. It should be noted that a layer on the interlayer surface corresponding to the  $\text{Al}_{12}\text{Mg}_{17}$  phase may also consist of Al. The morphology of the  $\text{Al}_{12}\text{Mg}_{17}$  interlayer surface, the walls of the cellular wall structure of the  $\text{Al}_3\text{Mg}_2$  phase interlayer surface and the Al surface were generally similar. It should also be noted that, at all interphase boundaries between the Al and Mg in the Al-Mg sample, the interlayer of the  $\text{Al}_3\text{Mg}_2$  intermetallic phase was wider than the interlayer of the  $\text{Al}_{12}\text{Mg}_{17}$

phase. These data were in good agreement with other results [46,47], where more detailed studies of the microstructure of these intermetallic phases were presented. In the current study, the width of the interlayer of the  $\text{Al}_3\text{Mg}_2$  phase was  $\approx 10\ \mu\text{m}$ , and the width of the  $\text{Al}_{12}\text{Mg}_{17}$  phase interlayer did not exceed  $3\ \mu\text{m}$ .

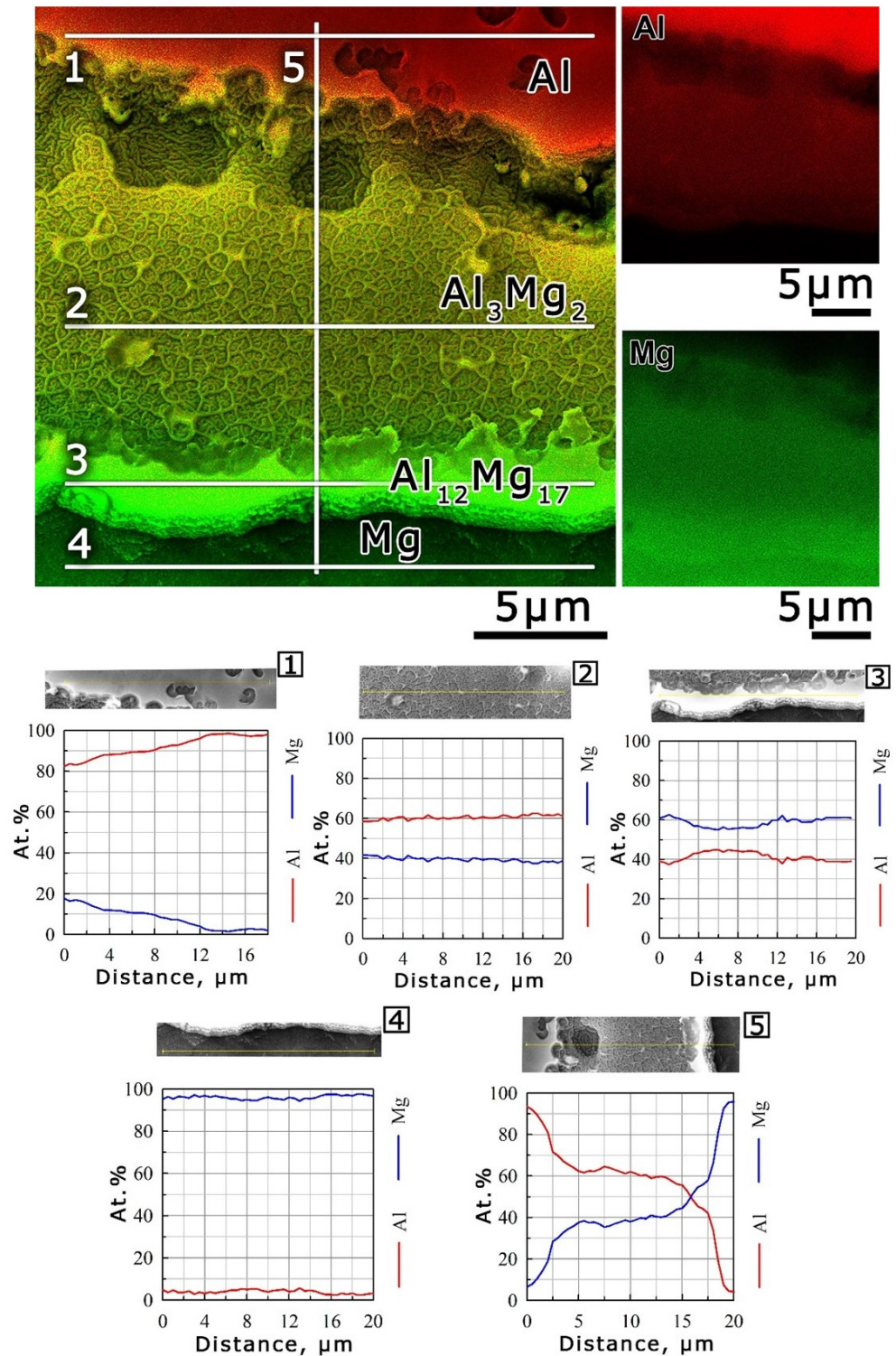


**Figure 5.** SEM image combined with an elemental map of the Al (in red) and Mg (in green). The element composition is shown along lines 1–5 at the top of the panel in the form of a relative intensity plot in relation to the scanning distance of the Al and Mg, marked in red and blue, respectively.

### 3.5. Sputtering Yield Evaluations

Figure 6 shows a 3D image and a profile of the Al-Mg sample surface after irradiation, measured with a NanoScan-3D in the atomic force microscopy (AFM) mode. The profile of the sample section is built relative to the initial surface level before the irradiation. The average depth of the etched areas corresponding to the Al matrix was 3.7  $\mu\text{m}$ , and it was 6.9  $\mu\text{m}$  for the Mg matrix. The smaller depth value of the Al-etched area was an indication of the lower sputtering rate of Al compared with that of Mg, and this was in agreement with the known data on the sputtering rates of these metals [48]. The depths of the etched sections of the interlayers corresponding to the  $\text{Al}_3\text{Mg}_2$  and  $\text{Al}_{12}\text{Mg}_{17}$  phases were 4.6 and 4.2  $\mu\text{m}$ , respectively. Therefore, the sputtering rates of these phases were between the sputtering rates of Al and Mg. In this case, the depth of the etched area of the  $\text{Al}_{12}\text{Mg}_{17}$  phase and, therefore, the sputtering rate of this phase were less than those of the  $\text{Al}_3\text{Mg}_2$  phase.

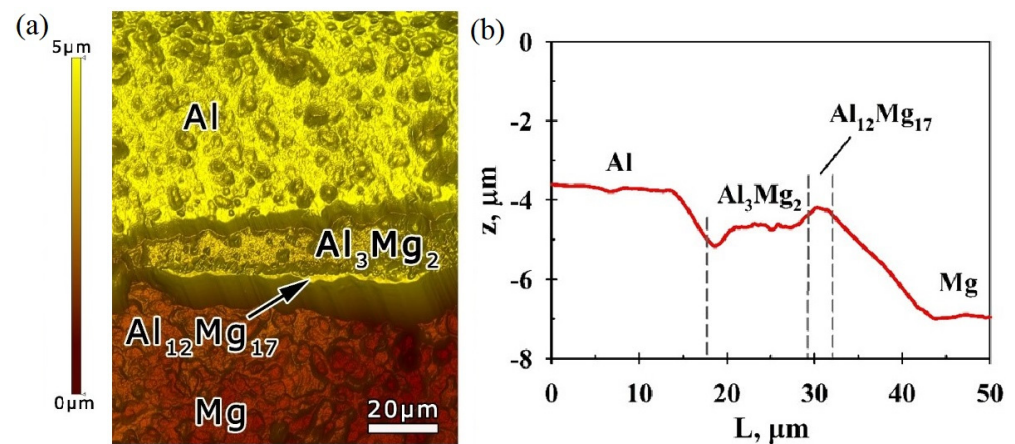


Figure 6. AFM image (a) and profile (b) of the Al-Mg composite surface after irradiation.

The sputtering yield of the  $\text{Al}_3\text{Mg}_2$  and  $\text{Al}_{12}\text{Mg}_{17}$  intermetallic phases was estimated following the expression used to determine the sputtering rate of metals:

$$\frac{z}{t} = \frac{Mj}{\rho N_a e} \cdot Y \quad (1)$$

where  $z/t$  is the sputtering rate;  $M$  is the metal molar weight;  $j$  is the ion current density;  $\rho$  is the density of the metal;  $N_a$  is the Avogadro constant;  $e$  is the electron charge; and  $Y$  is the sputtering yield [47]. Based on the fact that the irradiation conditions—in particular, the ion current density and the irradiation time—are the same (i.e.,  $j$ ,  $t$ ,  $N_a$  and  $e$  are constant), then the ratio of the sputtering yields,  $Y_1/Y_2$ , is proportional to the ratio of the depths of the etched areas,  $z_1/z_2$ , i.e.,

$$\frac{Y_1}{Y_2} = \frac{z_1}{z_2} \cdot \frac{M_2 \rho_1}{M_1 \rho_2} \quad (2)$$

The value of the sputtering yield ratio,  $Y_1/Y_2$ , for Al and Mg calculated from expression (2) was 0.75. Based on [49] and calculations from SRIM-2013 (Stopping and Range of Ions in Matter—a collection of software packages), which are focused on the calculation of many features of the transport of ions in matter [50], the sputtering yield,  $Y$ , of Al for argon ions at 5 keV was equal to two. The sputtering yield,  $Y$ , of Mg in the same conditions was equal to 2.6. The  $Y_1/Y_2$  ratio for Al and Mg, in this case, was 0.77, which was in good agreement with the experimental data.

In order to estimate the sputtering yields of intermetallic phases, the sputtering yield of Al was considered to be equal to two. For calculations, the known data on the density of these phases were utilized:  $\rho(\text{Al}_3\text{Mg}_2) = 2.25 \text{ g/cm}^3$  and  $\rho(\text{Al}_{12}\text{Mg}_{17}) = 2.09 \text{ g/cm}^3$ . The average molar mass for the phases was considered as follows:  $M(\text{Al}_3\text{Mg}_2) = 25.9 \text{ g/mol}$

and  $M(\text{Al}_{12}\text{Mg}_{17}) = 25.4$  g/mol. The calculated sputtering yields of the intermetallic phases, following Equation (2), were found to be  $Y(\text{Al}_3\text{Mg}_2) = 2.2$  and  $Y(\text{Al}_{12}\text{Mg}_{17}) = 1.9$ , respectively. As seen from the calculations, the sputtering yield of the  $\text{Al}_{12}\text{Mg}_{17}$  phase was even lower than that of the Al. At the same time, the sputtering yields of the  $\text{Al}_3\text{Mg}_2$  and  $\text{Al}_{12}\text{Mg}_{17}$  intermetallic phases, calculated using SRIM-2013, were 2.3 and 2.4, respectively.

To explain the reasons for the small (relative to Al) sputtering yield of the  $\text{Al}_{12}\text{Mg}_{17}$  intermetallic phase, it was important to consider the binding energies of atoms in this phase. The binding energy of an atom is the energy required to remove an atom from the surface of a material, and its value correlates with the sublimation energy. The sputtering yield depends on the surface binding energy ( $E$ ) as following  $Y \sim 1/E$ . It is believed that the higher the binding energy, the lower the sputtering yield. In particular, the binding energies in pure Al and Mg metals are 3.19 and 1.42 eV, respectively [51]. Following the AFM measurements presented above, the sputtering yield of Al was less than that of Mg. In the case of the intermetallic phases, the differences in their sputtering yields were most likely also due to differences in their binding energies.

The binding energies for the  $\text{Al}_{12}\text{Mg}_{17}$  intermetallic phase were calculated using the DFT method. The binding energies of pure Al and Mg were calculated for comparison purposes. The calculation of the atoms' binding energies was also planned for the  $\text{Al}_3\text{Mg}_2$  phase; however, it could not be carried out because of the large number of atoms in the lattice, as was the case for the WF calculation. Therefore, the  $\text{Al}_{30}\text{Mg}_{23}$  phase was subjected to calculation.

The surface binding energy [52] was defined as

$$E_{SBE} = E_{atom} + E_{SV} - E_S, \quad (3)$$

where  $E_S$  is the total energy of the slab with a clean surface, and  $E_{SV}$  denotes the total energy of the surface slab with a single surface vacancy. The surfaces with and without vacancy are relaxed.  $E_{atom}$  is the atomic energy of the removed species. The calculated values of the binding energy of atoms are presented in Table 4.

**Table 4.** The values of the binding energies in Al, Mg and the intermetallic phases  $\text{Al}_{12}\text{Mg}_{17}$  and  $\text{Al}_{30}\text{Mg}_{23}$  (close to  $\text{Al}_3\text{Mg}_2$ ), calculated via the DFT method.

Structure	Vacancy Type	Surface Binding Energy, eV	
Al	(001)	3.84	
	(111)	3.40	
Mg	(001)→(0001)	1.56	
	(111)→(11-21)	1.57	
$\text{Al}_{12}\text{Mg}_{17}$	(001)→(0001)	4.02	
		Mg	1.53
	(111)→(11-21)	Al	3.90
		Mg	1.71
$\text{Al}_{30}\text{Mg}_{23}$	(001)→(0001)	Al	2.86
		Mg	1.85
	(111)→(11-21)	Al	3.10
		Mg	1.85

The binding energy of atoms in pure Al was found to be higher than that of pure Mg, which was consistent with the known data. In the case of the  $\text{Al}_{12}\text{Mg}_{17}$  intermetallic phase, the removal of an Al atom from its surface requires an energy of 3.90–4.02 eV, which is, on average, higher than the binding energy of pure Al atoms of 3.40–3.84 eV. To remove Mg atoms from the surface of the same phase, an energy of 1.53–1.71 eV is required, which also

exceeds, on average, the binding energy of atoms in pure Mg, 1.56–1.57 eV. In the case of the  $\text{Al}_{30}\text{Mg}_{23}$  phase, the energy required to remove Al atoms from its surface was 2.86–3.10 eV, which is, on average, less than the binding energies of pure Al and the  $\text{Al}_{12}\text{Mg}_{17}$  phase. The binding energy of Mg for the same phase was 1.85 eV, which exceeded the binding energy of pure Mg, as well as the binding energy of Mg atoms for the  $\text{Al}_{12}\text{Mg}_{17}$  phase. Therefore, it can be concluded that the binding energy of the atoms in the  $\text{Al}_{12}\text{Mg}_{17}$  phase slightly exceeded the binding energy of atoms in Al, which was consistent with the estimated values of the sputtering yield.

### 3.6. Microhardness Measurements

Figure 7 shows an optical microscopy image of the Al-Mg composite surface taken from the non-irradiated side of the sample (Figure 7a), as well as after ion irradiation (Figure 7b). A different color contrast was noticed for Al, Mg and interlayers corresponding to the  $\text{Al}_3\text{Mg}_2$  and  $\text{Al}_{12}\text{Mg}_{17}$  intermetallic phases. The dark color contrast on the irradiated composite surface was related to the  $\text{Al}_3\text{Mg}_2$  phase and was the result of light from the incandescent lamp of an optical microscope (Figure 7b). This indicated the relatively high light absorption capacity of the  $\text{Al}_3\text{Mg}_2$  phase surface with a cellular wall relief. The Al areas and the interlayer corresponding to the  $\text{Al}_{12}\text{Mg}_{17}$  phase had the same light contrast. The area corresponding to the Mg surface, with cones located on it, had an orange-like contrast. The difference in contrast of these areas did not depend on the level of their depth relative to each other; rather, they depended only on their surface morphology and the optical properties of these metals and intermetallic phases.

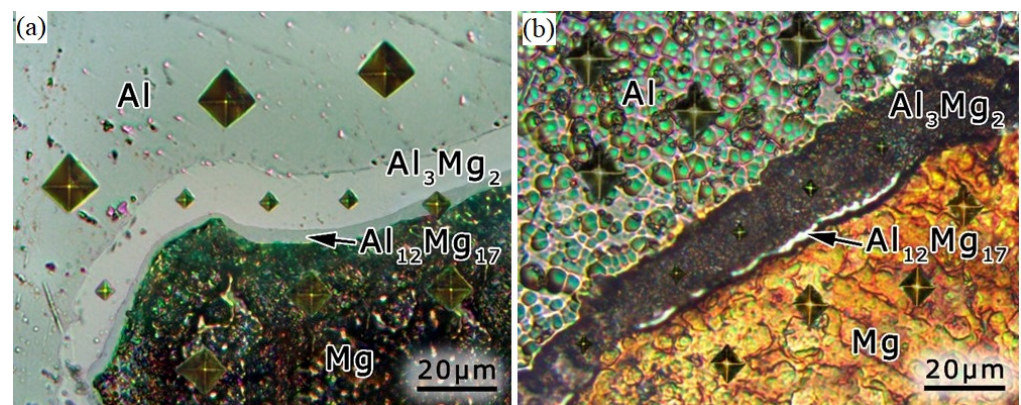


**Figure 7.** Optical image of the Al-Mg nanostructured composite surface before (a) and after (b) ion irradiation.

Microhardness measurements were carried out on the irradiated side of the Al-Mg sample. The microhardness value for Al was found to be  $55 \pm 10$  HV, and it was  $100 \pm 20$  HV for Mg,  $460 \pm 50$  HV for the  $\text{Al}_3\text{Mg}_2$  intermetallic phase and about 200 HV for the  $\text{Al}_{12}\text{Mg}_{17}$  phase. The microhardness values for the non-irradiated side of the Al-Mg composite were found to be as follows:  $50 \pm 10$  HV for Al,  $100 \pm 20$  HV for Mg,  $440 \pm 30$  HV for the  $\text{Al}_3\text{Mg}_2$  intermetallic phase and about 200 HV for the  $\text{Al}_{12}\text{Mg}_{17}$  phase. The imprints of the diamond pyramid obtained during the microhardness measurement are visible in Figure 7. The obtained microhardness values for Al and Mg, as well as for the  $\text{Al}_{12}\text{Mg}_{17}$  intermetallic phase on the non-irradiated side of the composite, were similar to the previously reported data. At the same time, the microhardness for the  $\text{Al}_3\text{Mg}_2$  phase, 460 HV on average, exceeded the known data for the microhardness of this phase (about 300 HV). However, the microhardness of the  $\text{Al}_3\text{Mg}_2$  phase had the highest value compared with the  $\text{Al}_{12}\text{Mg}_{17}$  phase, Al and Mg. It can also be seen that irradiation with argon ions and the corresponding change in the morphology on the surfaces of Al, Mg and intermetallic phases did not result in a microhardness change. This correlated with the results in [53], where no effect of Al irradiation with argon ions on microhardness was noticed.

#### 4. Conclusions

An Al-Mg metal-matrix composite was obtained via severe plastic deformation using high-pressure torsion at 5 GPa followed by annealing at a temperature of 275 °C. SEM, EDX and XRD studies showed that interlayers corresponding to the  $\text{Al}_3\text{Mg}_2$  and  $\text{Al}_{12}\text{Mg}_{17}$  intermetallic phases were formed at the Al and Mg interfaces. The sputtering yield of the  $\text{Al}_3\text{Mg}_2$  phase was found to be 2.2 atom/ion, while the sputtering yield of the  $\text{Al}_{12}\text{Mg}_{17}$  phase was found to be 1.9 at/ion, which is lower than those of Al (2 at/ion) and Mg (2.6 at/ion). The sputtering yield of the  $\text{Al}_{12}\text{Mg}_{17}$  phase did not follow the additivity rule for its constituent metals, as opposed to the  $\text{Al}_3\text{Mg}_2$  phase. To explain the differences in the sputtering yields, DFT-based simulations were used to calculate the surface-binding energy values for Al, Mg and the  $\text{Al}_{12}\text{Mg}_{17}$  phase. The values of the surface-binding energies of Al and Mg were in a range of 3.40–3.84 eV and 1.56–1.57 eV, respectively. The surface binding energy for the  $\text{Al}_{12}\text{Mg}_{17}$  phase with an Al atom removed from its surface was found to be in a range of 3.90–4.02 eV, and in a range of 1.53–1.71 eV with a Mg atom being removed. Optical microscopy analysis revealed that the  $\text{Al}_3\text{Mg}_2$  phase with a cellular wall surface morphology, which formed due to its irradiation with argon ions with an energy of 5 keV, had a high absorption capacity in the visible light spectrum relative to Al, Mg and the  $\text{Al}_{12}\text{Mg}_{17}$  phase. The WF of the obtained Al-Mg nanostructured composite was found to be 4 eV. This value was in a range between the WF values of Al (4.3 eV) and Mg (3.6 eV); i.e., the additivity rule was preserved. Using DFT-based simulations, the WF of the  $\text{Al}_{12}\text{Mg}_{17}$  phase was determined; its value was found to be in a range of 3.63–3.75 eV, which agrees with the additivity rule. Therefore, the intermetallic alloy based on  $\text{Al}_{12}\text{Mg}_{17}$ , with its relatively low sputtering yield and WF, was found to be promising as a cathode material for various gas-discharge devices, plasma installations, ion sources, sputtering systems, etc. The intermetallic alloy based on  $\text{Al}_3\text{Mg}_2$  with a modified surface was found to be a promising optical- and acoustic-absorbing material.

**Author Contributions:** Conceptualization, R.K.K., G.F.K., K.S.N. and R.R.M.; methodology, R.U.S., R.R.T. and Y.M.Y.; validation, G.R.K., G.F.K. and K.S.N.; formal analysis, A.A.K. and E.A.K.; investigation, R.K.K., A.A.K., G.R.K., R.U.S. and R.R.T.; writing—original draft preparation, R.K.K. writing—review and editing A.A.K., G.F.K. and E.A.K.; visualization, R.U.S.; supervision, R.R.M.; project administration, G.F.K. All authors have read and agreed to the published version of the manuscript.

**Funding:** The present work was accomplished according to the state assignment of IMSP RAS. SEM studies were performed using the equipment of the Center for Shared Access “Structural and Physicomechanical Investigations of Materials” at the Institute for Metal Superplasticity Problems of the Russian Academy of Sciences. E.A.K. acknowledges the support of Grant NSh-4320.2022.1.2 from the President of the Russian Federation for the state support of young Russian scientists—candidates of sciences and doctors of sciences. A.A.K. is grateful for financial support from the Ministry of Science and Higher Education of the Russian Federation within the framework of the state task of the UUST (No. 075-03-2023-119) of the youth research laboratory “Metals and Alloys under Extreme Impacts”. DFT simulations were carried out using the equipment of the shared research facilities of the Joint Supercomputer Center of the Russian Academy of Sciences.

**Institutional Review Board Statement:** Not applicable.

**Informed Consent Statement:** Not applicable.

**Data Availability Statement:** Not applicable.

**Acknowledgments:** The authors are grateful to Tatyana Konkova (University of Strathclyde, Glasgow, UK) for assistance in manuscript preparation (English editing).

**Conflicts of Interest:** The authors declare no conflict of interest.

## References

1. Wang, J.; Niu, L.; Zhang, Y.; Chen, J.; Jiang, J.; Song, D.; Li, B.; Ying, G.; Cheng, J.; Ma, A. Is Mg<sub>17</sub>Al<sub>12</sub> ductile or brittle? A theoretical insight. *J. Magnes. Alloy*. **2021**. [\[CrossRef\]](#)
2. Zhang, Q.; Zhu, Y.; Gao, X.; Wu, Y.; Hutchinson, C. Training high-strength aluminum alloys to withstand fatigue. *Nat. Commun.* **2020**, *11*, 5198. [\[CrossRef\]](#)
3. Nishimura, K.; Imai, K.; Matsuda, K.; Nunomura, N.; Tsuchiya, T.; Isikawa, Y.; Adachi, H.; Hutchison, W.D. Magnetic property of Al-Mg alloys and intermetallic compounds. *J. Alloys Compd.* **2021**, *877*, 160226. [\[CrossRef\]](#)
4. Thakur, A.; Kaya, S.; Kumar, A. Recent Trends in the Characterization and Application Progress of Nano-Modified Coatings in Corrosion Mitigation of Metals and Alloys. *Appl. Sci.* **2023**, *13*, 730. [\[CrossRef\]](#)
5. Kazakov, A.M.; Yakhin, A.V.; Karimov, E.Z.; Babicheva, R.I.; Kistanov, A.A.; Korznikova, E.A. Effect of Segregation on Deformation Behaviour of Nanoscale CoCrCuFeNi High-Entropy Alloy. *Appl. Sci.* **2023**, *13*, 4013. [\[CrossRef\]](#)
6. Bihari, B.; Singh, A.K. An Overview on Different Processing Parameters in Particulate Reinforced Metal Matrix Composite Fabricated by Stir Casting Process. *IJERA* **2017**, *7*, 42–48. [\[CrossRef\]](#)
7. Mehr, V.Y.; Toroghinejad, M.R.; Rezaeian, A. Mechanical properties and microstructure evolutions of multilayered Al–Cu composites produced by accumulative roll bonding process and subsequent annealing. *Mater. Sci. Eng.* **2014**, *601*, 40–47. [\[CrossRef\]](#)
8. Fronczek, D.; Chulist, R.; Litynska-Dobrzynska, L.; Kac, S.; Schell, N.; Kania, Z.; Szulc, Z.; Wojewoda-Budka, J. Microstructure and kinetics of intermetallic phase growth of three-layered A1050/AZ31/A1050 clads prepared by explosive welding combined with subsequent annealing. *Mater. Des.* **2017**, *130*, 120–130. [\[CrossRef\]](#)
9. Keiichiro, O.; Edalati, K.; Kim, H.S.; Hono, K.; Horita, Z. High-pressure torsion for enhanced atomic diffusion and promoting solid-state reactions in the aluminum–copper system. *Acta Mater.* **2013**, *61*, 3482–3489. [\[CrossRef\]](#)
10. Korznikova, E.A.; Mironov, S.Y.; Korznikov, A.V.; Zhilyaev, A.P.; Langdon, T.G. Microstructural evolution and electro-resistivity in HPT nickel. *Mater. Sci. Eng.* **2012**, *556*, 437–445. [\[CrossRef\]](#)
11. Bouaziz, O.; Kim, H.S.; Estrin, Y. Architecturing of Metal-Based Composites with Concurrent Nanostructuring: A New Paradigm of Materials Design. *Adv. Eng. Mater.* **2013**, *15*, 336. [\[CrossRef\]](#)
12. Zhilyaev, A.; Langdon, T. Using high-pressure torsion for metal processing: Fundamentals and applications. *Prog. Mater. Sci.* **2008**, *53*, 893–979. [\[CrossRef\]](#)
13. Mulyukov, R.R.; Korznikova, G.F.; Nazarov, K.S.; Khisamov, R.K.; Sergeev, S.N.; Shayakhmetov, R.U.; Khalikova, G.R.; Korznikova, E.A. Annealing-induced phase transformations and hardness evolution in Al–Cu–Al composites obtained by high-pressure torsion. *Acta Mech.* **2021**, *232*, 1815–1828. [\[CrossRef\]](#)
14. Korznikova, G.; Kabirov, R.; Nazarov, K.; Khisamov, R.; Shayakhmetov, R.; Korznikova, E.; Khalikova, G.; Mulyukov, R. Influence of Constrained High-Pressure Torsion on Microstructure and Mechanical Properties of an Aluminum-Based Metal Matrix Composite. *JOM* **2020**, *72*, 2898–2911. [\[CrossRef\]](#)
15. Sun, Y.; Aindow, M.; Hebert, R.J.; Langdon, T.G.; Lavernia, E.J. High-pressure torsion-induced phase transformations and grain refinement in Al/Ti composites. *J. Mater. Sci.* **2017**, *52*, 12170. [\[CrossRef\]](#)
16. Bartkowska, A.; Bazarinik, P.; Huang, Y.; Lewandowska, M.; Langdon, T.G. Using high-pressure torsion to fabricate an Al–Ti hybrid system with exceptional mechanical properties. *Mater. Sci. Eng.* **2021**, *799*, 140114. [\[CrossRef\]](#)
17. Kawasaki, M.; Han, J.-K.; Lee, D.-H.; Jang, J.-I.; Langdon, T.G. Fabrication of nanocomposites through diffusion bonding under high-pressure torsion. *J. Mater. Res.* **2018**, *33*, 2700–2710. [\[CrossRef\]](#)
18. Korznikova, G.F.; Korznikova, E.A.; Khalikova, G.R.; Nazarov, K.S.; Khisamov, R.K.; Sergeev, S.N.; Shayakhmetov, R.U.; Mulyukov, R.R. Al based layered in situ metal-matrix composites fabricated by constrained high pressure torsion. *Lett. Mater.* **2021**, *11*, 533–543. [\[CrossRef\]](#)
19. Korznikova, G.; Korznikova, E.; Nazarov, K.; Shayakhmetov, R.; Khisamov, R.; Khalikova, G.; Sergeev, S.; Mulyukov, R. Structure and mechanical behavior of Al–Nb hybrids obtained by high-pressure-torsion-induced diffusion bonding and subsequent annealing. *Adv. Eng. Mater.* **2021**, *23*, 2000757. [\[CrossRef\]](#)
20. Patel, M.; Pardhi, B.; Pal, M.; Singh, M.K. SiC Particulate Reinforced Aluminium Metal Matrix Composite. *Adv. J. Grad. Res.* **2018**, *5*, 8–15. [\[CrossRef\]](#)
21. Lapin, S.; Ivanisenko, Y.; Kilmametov, A.; Valiev, R. High pressure torsion of aluminum and aluminum oxide powders: Fabrication and properties of a metal matrix composite. *Mater. Sci. Eng. A* **2014**, *606*, 277–284. [\[CrossRef\]](#)
22. Ma, Y.; Liu, H.; Wu, X.; Wu, Y.; Lu, J. Enhanced mechanical properties and wear behavior of Al-Mg alloys reinforced with TiB<sub>2</sub> nanoparticles. *Mater. Sci. Eng. A* **2014**, *620*, 28–35. [\[CrossRef\]](#)
23. Kulkova, S.E.; Straumal, B.B.; Kucheev, Y.O.; Czeppe, T.; Baretzky, B. Fabrication and characterization of aluminum-graphene oxide composites by high-pressure torsion. *Mater. Sci. Eng. A* **2016**, *667*, 130–137. [\[CrossRef\]](#)
24. Sadrnezhaad, S.K.; Yazdani, S.; Kokabi, A.H.; Toroghinejad, M.R. Enhancement of mechanical properties of Al–SiC composite processed by high-pressure torsion. *Mater. Sci. Eng. A* **2008**, *477*, 67–71. [\[CrossRef\]](#)
25. Ramezani, M.; Sajjadi, S.A.; Rezayat, M.; Kim, H.S.; Lee, M.G. High-pressure torsion processing of aluminum-based nanocomposites reinforced with carbon nanotubes. *Mater. Des.* **2014**, *63*, 732–739. [\[CrossRef\]](#)
26. Cho, Y.H.; Jung, J.H.; Lee, H.S.; Lee, C.S.; Kim, N.J. Microstructure and mechanical properties of aluminum matrix composite reinforced with alumina particles fabricated by high-pressure torsion. *J. Mater. Sci. Technol.* **2015**, *31*, 925–931. [\[CrossRef\]](#)

27. Gwalani, B.; Sahajwalla, V.; Joshi, R.K.; Khanna, R.; Balani, K. Strengthening and wear resistance of Al-Mg alloys through high-pressure torsion and SiC reinforcement. *J. Mater. Res.* **2017**, *32*, 3338–3346. [CrossRef]
28. Abd El Aal, M.I.; El-Fahhar, H.H.; Mohamed, A.Y.; Gadallah, E.A. The Mechanical Properties of Aluminum Metal Matrix Composites Processed by High-Pressure Torsion and Powder Metallurgy. *Materials* **2022**, *15*, 8827. [CrossRef]
29. Momeni, M.; Loh-Mousavi, S.; Haghdadadi, N.; Baghchesara, M.A.; Akbarpour, M.R. Effect of high-pressure torsion on the microstructure and mechanical properties of an Al matrix composite reinforced with Si<sub>3</sub>N<sub>4</sub> particles. *J. Mater. Sci. Technol.* **2020**, *44*, 87–94. [CrossRef]
30. Zhang, W.; Yuan, F.; Yang, J.; Liu, Y.; Zhang, L. Microstructure and mechanical properties of Al matrix composites reinforced with TiN nanoparticles prepared by high-pressure torsion. *Mater. Sci. Eng. A* **2020**, *771*, 138586. [CrossRef]
31. Liu, L.M.; Wang, H.Y.; Zhang, Z.D. The analysis of laser weld bonding of Al alloy to Mg alloy. *Scr. Mater.* **2007**, *56*, 473–476. [CrossRef]
32. Kostka, A.; Coelho, R.S.; dos Santos, J.; Pyzalla, A.R. Microstructure of friction stir welding of aluminium alloy to magnesium alloy. *Scr. Mater.* **2009**, *60*, 953–956. [CrossRef]
33. Dietrich, D.; Nickel, D.; Krause, M.; Lampke, T.; Coleman, M.P.; Randle, V. Formation of intermetallic phases in diffusion-welded joints of aluminium and magnesium alloys. *J. Mater. Sci.* **2010**, *46*, 357–364. [CrossRef]
34. Zisman, W.A. A new method of measuring contact potential difference in metals. *Rev. Sci. Instruments* **1932**, *3*, 367. [CrossRef]
35. Klein, U.; Vollmann, W.; Abatti, P.J. Contact potential differences measurement: Short history and experimental setup for classroom demonstration. *IEEE Trans. Educ.* **2003**, *46*, 338–344. [CrossRef]
36. Khisamov, R.K.; Khalikova, G.R.; Kistanov, A.A.; Korznikova, G.F.; Korznikova, E.A.; Nazarov, K.S.; Sergeev, S.N.; Shayakhmetov, R.U.; Timiryayev, R.R.; Yumaguzin, Y.M.; et al. Microstructure, microhardness and work function of in-situ Al-Cu composite processed by mechanical alloying by means of high-pressure torsion. *Contin. Mech. Thermodyn.* **2022**. [CrossRef]
37. Kresse, G.; Furthmüller, J. Efficient iterative schemes for ab initio total-energy calculations using a plane-wave basis set. *Phys. Rev. B Cond. Mater.* **1996**, *54*, 11169–11186. [CrossRef]
38. Arisova, V.N.; Trykov, Y.P.; Slautin, O.V.; Ponomareva, I.A.; Kondakov, A.E. Effect of heat treatment on mechanical properties and phase composition of magnesium aluminum composite prepared by explosive welding. *Met. Sci. Heat Treat.* **2015**, *57*, 291–294. [CrossRef]
39. Fomenko, F.S. *Emission Properties of Materials*, 3rd ed.; Joint Publications Research Service: Arlington, VA, USA, 1972; p. 172.
40. Michaelson, H.B. The work function of the elements and its periodicity. *J. Appl. Phys.* **1977**, *48*, 4729–4733. [CrossRef]
41. Kawano, H. Effective Work Functions of the Elements: Database, Most probable value, Previously recommended value, Polycrystalline thermionic contrast, Change at critical temperature, Anisotropic dependence sequence, Particle size dependence. *Prog. Surf. Sci.* **2022**, *97*, 100583. [CrossRef]
42. Khisamov, R.K.; Safarov, I.M.; Mulyukov, R.R.; Yumaguzin, Y.M.; Zubairov, L.R.; Nazarov, K.S. Effect of formation of a nanocrystalline structure on the electron work function and ion-electron emission of nickel. *Tech. Phys.* **2011**, *56*, 1661–1664. [CrossRef]
43. Tang, K.; Du, Q.; Li, Y. Modelling microstructure evolution during casting, homogenization and ageing heat treatment of Al-Mg-Si-Cu-Fe-Mn alloys. *Calphad* **2018**, *63*, 164–184. [CrossRef]
44. Jain, A.; Ong, S.P.; Hautier, G.; Chen, W.; Richards, W.D.; Dacek, S.; Cholia, S.; Gunter, D.; Skinner, D.; Ceder, G.; et al. The Materials Project: A materials genome approach to accelerating materials innovation. *APL Mater.* **2013**, *1*, 011002. [CrossRef]
45. Carter, G.; Katardjiev, I.V.; Nobes, M.J.; Whitton, J.L. Sputtering-induced surface topography on F.C.C. metals. *Mater. Sci. Eng.* **1987**, *90*, 21–32. [CrossRef]
46. Shahid, R.N.; Scudino, S. Microstructure and Mechanical Behavior of Al-Mg Composites Synthesized by Reactive Sintering. *Metals* **2018**, *8*, 762. [CrossRef]
47. Tayyebi, M.; Adhami, M.; Karimi, A.; Rahmatabadi, D.; Alizadeh, M.; Hashemi, R. Effects of strain accumulation and annealing on interfacial microstructure and grain structure (Mg and Al<sub>3</sub>Mg<sub>2</sub> layers) of Al/Cu/Mg multilayered composite fabricated by ARB process. *J. Mater. Res. Technol.* **2021**, *14*, 392–406. [CrossRef]
48. Available online: <https://www.angstromsciences.com/sputtering-yields> (accessed on 1 January 2021).
49. Behrish, R.; Eckstein, W. *Sputtering by Particle Bombardment*; Springer: Berlin/Heidelberg, Germany, 2007; pp. 1–509. [CrossRef]
50. Ziegler, J. SRIM and TRIM. Available online: <http://www.srim.org/> (accessed on 1 January 2021).
51. Kudriavtsev, Y.; Villegas, A.; Godines, A.; Asomoza, R. Calculation of the surface binding energy for ion sputtered particles. *Appl. Surf. Sci.* **2005**, *239*, 273–278. [CrossRef]
52. Gyoerok, M.; Kaiser, A.; Sukuba, I.; Urban, J.; Hermansson, K.; Probst, M. Surface binding energies of beryllium/tungsten alloys. *J. Nucl. Mater.* **2016**, *472*, 76–81. [CrossRef]
53. Bizyukov, I.; Girka, O.; Kaczmarek, Ł.; Klich, M.; Myroshnyk, M.; Januszewicz, B.; Owczarek, S. Aluminium and titanium alloys surface behaviour under argon and helium ion exposure. *NIMB* **2018**, *436*, 272–277. [CrossRef]

**Disclaimer/Publisher’s Note:** The statements, opinions and data contained in all publications are solely those of the individual author(s) and contributor(s) and not of MDPI and/or the editor(s). MDPI and/or the editor(s) disclaim responsibility for any injury to people or property resulting from any ideas, methods, instructions or products referred to in the content.